Boundary-Layer Meteorology
https://doi.org/10.1007/s10546-022-00698-6

RESEARCH ARTICLE

Momentum and Turbulent Transport in Sparse, Organized Vegetative Canopies

Gregory Torkelson[1] · **Timothy A. Price**[1] · **Rob Stoll**[1]

Received: 21 October 2021 / Accepted: 22 February 2022

Abstract
The effect of canopy heterogeneity on mean and turbulent transport processes is studied using a scaled wind-tunnel model of a vineyard canopy with gap spacings of one, two, and three canopy heights. A row-normal freestream velocity component is applied to each canopy configuration and spatial distributions of velocity across a streamwise-vertical plane centred around a single canopy gap are measured using particle imaging velocimetry. Mean flow features including an updraft in the centre of the canopy followed by a descent and recirculation just upstream of the downstream row are observed to decrease in size and magnitude for larger canopy gaps. Turbulence in the canopy sublayer (CSL) is dominated by a growing mixing layer that originates at the top of the upstream row and consumes the underlying weak more isotropic turbulence. The mixing layer's rate of growth into the CSL decreases as the canopy gap widens, but not enough to offset the increased downstream distance. The vertical extent of the mixing layer into the canopy before being impeded by the downstream row is the main factor that determines horizontal heterogeneity of turbulence in the canopy. An analysis of the Reynolds-averaged turbulence-kinetic-energy budget points to shear production being the main source of turbulence near the canopy top, while turbulent transport is responsible for the growth of the mixing layer down into the CSL.

Keywords Canopy flow · Particle image velocimetry · Turbulence kinetic energy · Wind tunnel

1 Introduction

Vegetative canopies play a critical role in the exchange of energy and mass between the atmosphere and the surface of the Earth. A key component of this exchange is the transport of fluid momentum and scalars by turbulence. Although the structure of vegetative canopies is extremely diverse, a significant portion of research characterizing the flow and turbulence within and above plant canopies has focused on horizontally homogeneous canopies, with heterogeneous canopies only recently seeing significant emphasis (see Finnigan 2000; Brunet 2020, and references therein). The work on homogeneous canopies has significantly

✉ Rob Stoll
rstoll@eng.utah.edu

[1] University of Utah Mechanical Engineering, 1495 E 100 S MEK 1550, Salt Lake City, Utah 84112, USA

advanced our understanding of turbulent transport in and above plant canopies, leading to the development of the canopy-mixing-layer analogy (Raupach et al. 1996), the identification of a spectral shortcut (Kaimal and Finnigan 1994; Poggi et al. 2004), and the application of a volume-averaging operator to Reynolds-averaged first- and second-moment budgets (Raupach and Shaw 1982). In addition, other researchers examined homogeneous canopies with the aim of unifying some of the above theories and merging them with atmospheric boundary-layer and surface-layer theory (Garratt 1980; Cellier and Brunet 1992; Poggi et al. 2004; Harman and Finnigan 2007).

The volume-averaged turbulence-kinetic-energy (TKE) budget in particular has been used to understand how energy generated through canopy shear is transported and balanced by canopy element drag (Brunet et al. 1994; Yue et al. 2008). Most of this work focused on the vertical distribution of TKE budget terms, with the associated horizontal distributions receiving very little attention due to the difficulties of obtaining accurate spatial measurements around vegetation elements. The work that has been done on the horizontal variability of TKE budget terms has mostly been performed in canopies of bluff objects, e.g., urban canopies (Giometto et al. 2016; Blackman et al. 2017).

The shift in canopy-flow research towards flow dynamics within and around heterogeneous and sparse canopies is relatively recent and has been pursued using a combination of numerical simulations, field experiments, and laboratory experiments (LeMone et al. 2019; Brunet 2020; Stoll et al. 2020). Wind-tunnel and water-flume experiments have been a continuous part of these efforts. One of the earliest laboratory experiments was carried out by Novak et al. (2000), who uniformly removed trees from a model wind-tunnel canopy to examine the impact of canopy density on turbulent flow statistics. They found that, as density decreases, the spacing between canopy elements becomes increasingly important in establishing a horizontal length scale that affects turbulence in the canopy sublayer (CSL). Later, Böhm et al. (2013) detailed a series of experiments using an array of globes spaced to create conditions similar to sparse vegetation. The results showed aspects of both CSL flow and inertial sublayer (ISL) behaviour hypothesized to be a result of the distinct wake and no-wake regions unique to heterogeneous canopy flow. Böhm et al. (2013) looked at space–time averaged quantities using hotwire probes and did not resolve instantaneous spatial flow fields or recirculating features, which limited the interpretation of the data. Harman et al. (2016) later used bluff tombstone style elements similar in effect to the globes of Böhm et al. (2013) to simulate a canopy roughness layer. These experiments used three-dimensional laser Doppler velocimetry to produce three-dimensional vectors within a small flow volume. The results highlighted the need to quantify the microscale variability and dispersive stresses, which were shown to contribute significantly to the overall energy budget within the canopy in cases where coherent variation in the mean flow occurred. Poëtte et al. (2017) used the same experimental set-up as Harman et al. (2016) to investigate the impact of forest gaps on momentum transport. Their study can be viewed as an extreme case of sparse-canopy flow where the canopy is clumped into regions separated by clearings. They found that increased fragmentation of their modelled forest results in decreased average momentum absorption but localized spikes in turbulent stress and kinetic energy, emphasizing the impact of horizontal heterogeneity on local canopy flow dynamics.

Although not technically plant canopy flows, windbreak and urban flow studies have also advanced the understanding of the spatial flow structure of heterogeneous canopies. Based on a series of wind-tunnel experiments, Judd et al. (1996) identified the primary flow features present on the lee side of a windbreak. Regions downstream, including the bleed flow, mixing zone, and quiet zone, were mapped with enough detail to create a basic wind-flow model (Speckart and Pardyjak 2014). Similar flow patterns and zones have also been described

for isolated trees (Margairaz et al. 2022) and forest edges (Dupont and Brunet 2008), but an understanding of how these features are altered by the interaction with other canopy elements is still developing. Despite the presence of impermeable elements, the vertical structure of turbulence in urban flows is very similar to a vegetative canopy with the formation of a CSL near the canopy elements, a roughness sublayer (RSL) above the canopy, and the ISL far from the canopy (Britter and Hanna 2003). Because buildings are impermeable, horizontal heterogeneity is a common focus of urban flow studies. Many times this is through the examination of specific urban-canopy geometry features (e.g., street canyons, Addepalli and Pardyjak 2013; Park et al. 2020) with researchers finding similar but exaggerated flow zones to those found around windbreaks and isolated trees (Hayati et al. 2019; Park et al. 2020).

The limitations faced by Böhm et al. (2013) and Harman et al. (2016) (among others) can partially be resolved using particle imaging velocimetry (PIV). Zhu et al. (2006) and Van Hout et al. (2007) deployed a PIV system in a mature corn field and observed anisotropy at small scales at all heights in the canopy supporting the existance of a spectral shortcut. Lee and Lee (2012) used small fir-tree branches in a wind tunnel to model a row of trees, and made PIV measurements to quantify the sheltering effect within the wake of these model trees. Their analysis, however, did not focus on the role of geometric variations or any turbulence characteristics within the wake. Bai et al. (2012, 2015) used PIV to study the flow structure inside a complex canopy of multiscale elements using intricate model canopies designed to determine the role of fractal geometry on flow statistics. They used horizontal slices of PIV and traversed the plane vertically to build up ensemble-averaged three-dimensional fields. The results showed strong dispersive fluxes inside the canopy in agreement with Harman et al. (2016). The study of Bai et al. (2015) focused on multiscale effects but did not look at the spacing of organized row elements or the effects of individual dominant length scales. Hamed et al. (2020) used PIV to explore how the spatial structure of turbulence varies with gap width within canopy clearings. They discovered a flow transition from a skimming-flow regime, where the shear layer at the top of a canopy gap does not grow, to a shear-growth regime, which experiences considerable growth when the gap width increased similar to the regimes identified in urban flows (e.g., Hussain and Lee 1980).

The present work is focused on complex heterogeneous canopies that are sparse and organized with element spacing on the order of the canopy height. Examples of these types of canopies include grape vineyards, fruit orchards, and early development annual crops (Dry 2000). Using PIV measurement techniques and a model canopy placed in a wind tunnel, we examine the structure of the velocity field for different canopy configurations, and investigate how the balance of terms in the TKE equation and turbulent interactions within the CSL depend on canopy-element spacing.

2 Experimental Methods

2.1 Wind Tunnel

To examine the impact of sparse-canopy geometry on momentum transport, a wind-tunnel experiment was designed using modelled vegetative canopies. Experiments were conducted in the 7.9 m long (x) $\times$ 0.61 m tall (z) $\times$ 0.91 m wide (y) wind tunnel located at the University of Utah. The upstream flow speed was held constant at 5 m s^{-1} while the freestream flow speed above the canopy varied slightly between canopy configurations. The floor of the wind tunnel was covered with square LEGO^{TM} baseplate mats (LEGO^{TM} item 10700)

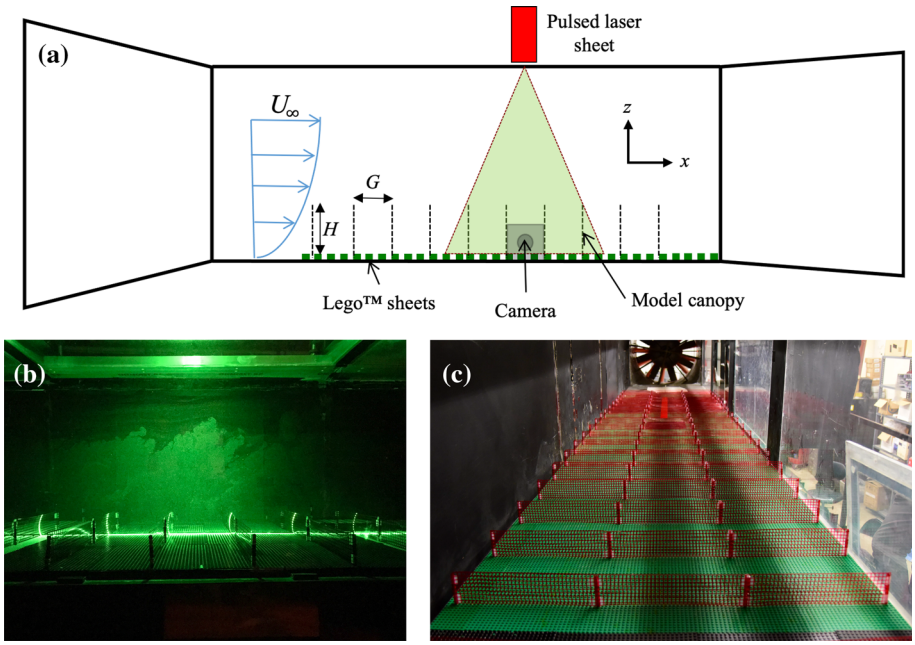

Fig. 1 Wind-tunnel experimental set-up: **(a)** schematic diagram of primary experimental components (not to scale), **(b)** PIV camera point of view during pre-mixed conditions, and **(c)** downstream view of the full canopy

containing roughness elements measuring 1.7 mm high with a 4.8-mm diameter spaced 8 mm on centre. Particle imaging velocimetry and pitot-static tube measurements were taken 5.9 m downwind of a 4-mm turbulence tripwire, 5.6 m into the test section, and 4.5 m from the start of the roughness elements. Pressure balance within the wind tunnel was verified and adjusted as necessary with and without the canopy installed. The coordinate system used below is defined by the u velocity component aligning with the streamwise x direction (normal to the rows), the v velocity component aligning with the spanwise y direction, and the w velocity component with the vertical z direction normal to the wall (Fig. 1).

2.2 Model Canopy

A critical component of our wind-tunnel investigation was the design of a scaled-canopy model that could represent practical arrangements of realistic sparse, organized canopies (e.g., trellised crops) while allowing flexibility to explore the impact of row spacing on momentum transport. For all canopy configurations rows spanned the full width of the wind tunnel (877 mm) and were 72 mm tall (H) and 0.13 mm thick (Fig. 1). The height was chosen as an integer of the LEGO^{TM} baseplate element spacing to enable the rows to be spaced at integers of the canopy height. Each row was made from transparent red film (Grafix coloured clear-lay film P/N 1827549MA) chosen so that scattered red light could be filtered out of the image with a yellow lens filter improving the image quality near the canopy rows. An approximately constant leaf area density was specified for each row using a uniform mesh with 52.8% optical porosity. Understorey space (common in vegetative canopies) was not

Table 1 Bulk flow and measurement statistics for each sparse-organized canopy wind-tunnel experiment

Row Spacing	$C_D \times LAI$	U_∞ (m s^{-1})	δ_{99}/H	u_* (m s^{-1})	Re_*	Image Pairs
$1H$	2.62	5.20	4.43	0.44	9357	2500
$2H$	1.63	4.76	5.11	0.45	11012	5000
$3H$	1.00	4.79	4.90	0.45	10451	2498

included so as simplify the analysis and increase the rigidity of canopy rows. The mesh consisted of a 6-mm square pattern spaced 2 mm on centre cut out with a Silhouette Cameo 3 cutting machine (Silhouette America, Inc., Lindon, Utah). The lowest square was replaced with a 6 mm wide 2 mm tall cut to provide the desired canopy density while maintaining integer canopy spacing. The modification to the cut pattern is expected to have minimal impact on canopy flow statistics since the flow speed reaches near zero close to the surface.

Rows were spaced at $1H$, $2H$, and $3H$. A bare-tunnel rough-wall boundary-layer dataset was also collected for statistical comparison. To ensure that turbulence statistics reached quasi-equilibrium within the test row, rows were placed upstream as far as possible. This leads to an upstream distance from the first row to the test row of 1.5 m for the $1H$ case and 3.3 m for the $2H$ and $3H$ cases. In all cases, rows were also positioned at the test case interval (e.g., $1H$) up to a distance of 0.5 m downwind of the test row to avoid any edge effects. The rows were fastened onto the LEGO^{TM} baseplate mats with slender LEGO^{TM} rods composed of seven, round brick, 9.6 mm high transparent red blocks (LEGO^{TM} element 3006841). Table 1 gives an overview of the experimental canopy configurations and resulting bulk statistics, including the total momentum absorption of the canopy $C_D \times LAI$ where C_D is the drag coefficient and LAI is the leaf area index, the freestream flow speed U_∞, the boundary-layer height δ_{99}, the ensemble- and spatially-averaged friction velocity $u_* = \left[-\overline{\langle u'w' \rangle}\right]^{\frac{1}{2}}$ (taken in the constant shear layer above the canopy), and the friction Reynolds number $Re_* = u_* \delta_{99} \nu^{-1}$ where ν is the kinematic viscosity of air. In the aforementioned, the angle brackets ($\langle\ \rangle$) indicate a spatial average, the overbar ($-$) indicates an ensemble average, and fluctuations, calculated as deviations from the plane-averaged mean value at each vertical height, are denoted by a prime ($'$). Also given is the number of quality-controlled instantaneous realizations taken (image pairs). The total momentum absorption parameter ($C_D \times LAI$) was estimated by vertically integrating the steady-state high-Re one-dimensional momentum equation over the canopy depth using the streamwise and ensemble-averaged velocity and vertical momentum-flux profiles (Cionco 1965). Assuming $C_D = 0.5$ results in LAI values of 1.31, 0.81, and 0.52 for the $1H$, $2H$, and $3H$ cases, respectfully, in agreement with the range of values observed in commercial vineyards (Johnson et al. 2003). The freestream velocity and boundary-layer heights were determined through pitot-static tube measurements, while u_* was calculated using the PIV measurements.

2.3 Particle Imaging Velocimetry Procedure

Instantaneous two-dimensional velocity vectors were acquired across a streamwise-vertical plane (x-z) located in and above the canopy using the PIV technique (Fig. 1). The measurement system consisted of a 14-bit greyscale camera (PowerViewTM 29MP, TSI Inc., Minnesota, USA) and a 150 mJ synchronized pulsed laser with sheet optics. The system has a sampling rate of up to 1.6 Hz; for the flow speed and length scales examined here, each

captured image pair should be considered as statistically independent. In order to converge turbulent statistics of interest, it is important that enough of these independent samples are recorded for each test case. Previous PIV canopy-flow studies used 2360 (Yue et al. 2008), 1000 (Moltchanov et al. 2011), 5000 (Hong et al. 2011), 2000 (Bai et al. 2015), and 4000 (Hamed et al. 2017) image pairs for each configuration, although justification of statistical convergence for any of these publications is minimal. In this study a minimum of 2500 samples was taken for each test case, with the middle row spacing ($2H$) increased to 5000 to test statistical convergence. No change in the values and distributions of the ensemble-averaged streamwise-vertical momentum flux was found between 2500 and 5000 frames.

The PIV technique relies on illuminating small particles in the flow that are assumed to be passive tracers. The tracer particles were created using two Laskin atomizer nozzles with extra virgin olive oil as the aerosol. Particle characterization with a laser particle spectrometer (1.108, Grimm Aerosol Technik, Ainring, Germany). indicated a mean aerodynamic diameter of 0.45 μm, well within the accepted size range (Melling 1997). The wind tunnel is an open return design; therefore, the entire laboratory room was seeded with aerosol for 15 min prior to running each experiment and the aerosol concentration within the wind tunnel was actively monitored using a TSI DustTrak^{TM} Model 8520. Experiments were run at several measured concentration values to quantify the required particle counts for optimal PIV vector quality. Based on these measured concentrations, acceptable operating bounds were set and the aerosol generation was adjusted during the experiment to maintain peak seeding quality.

System calibration was performed using the TSI Insight 4G^{TM} (version 10.1.0.1) software and a calibration target aligned with the laser sheet. After calibration, test images were processed through a dewarping algorithm to correct any minor misalignment between the laser sheet plane, calibration plane, and the camera field-of-view. The camera and laser were rigidly fastened in place on the wind-tunnel structure to prevent any movement and drift in the calibration and the focus of the camera was carefully verified prior to every experiment. Finally, the viewing window and transparent ceiling were cleaned both inside and outside before every experiment to minimize contaminated data due to streaks and dust within the field-of-view or laser path. A narrow strip of reflective red tape was placed on the floor within the PIV field-of-view to maximize measurement quality near the wall and reduce laser light scatter.

Our sparse-canopy flow experiment is characterized by low-magnitude velocity flow inside the canopy transitioning to a relatively high-magnitude velocity above, and therefore, the PIV settings must be optimized to capture both regions of the flow. Here, we used a rectangular interrogation region of 20 pixels in the vertical direction by 36 pixels in the streamwise and a time delay between image acquisitions of 130 μs to minimize sub-pixel particle displacements in low-velocity areas while maintaining maximum particle displacement of less than 30% of the interrogation window size. The processing within Insight 4G^{TM} used a recursive deformation grid procedure with an initial interrogation region of 40×72 pixels and a final interrogation region of 20×36 pixels, resulting in a vector resolution of 361×435 with a vector pitch of 1.26 mm in the x and 0.7 mm in the z directions.

The vector quality was evaluated for each independent velocity field during postprocessing. Turbulent statistics calculated using velocity vectors within three vector pitches of the surface and rows were determined to be non-physical likely as a result of light scattering and were subsequently removed. Image pairs with less than 90% good vectors (as determined through Insight 4G^{TM}) were then removed, resulting in the number of image pair shown in Table 1. Generally data quality inside the canopy bounds was good with very few overall removed frames, but extreme velocity outliers were still prevalent in some areas of the flow. Multiple methods of removing non-physical velocity vectors inside the canopy were

attempted and best results were found through a two-step methodology. First, nine small areas ranging in size from 1×2 vectors to 4×4 vectors were identified manually. In these areas, corrupted vectors occurred in an average of 26.4% of the frames and were found to affect velocity moments and TKE. Frames with corrupted vectors were identified by either velocity component having a deviation larger than 0.2 m s^{-1} from a local mean determined by spatial averaging the surrounding three vectors in each direction. For these specifically identified areas removal of vectors caused a loss of local data quality due to insufficient ensemble samples and therefore, bad vectors were simply replaced with the local mean instead of removed. After this first pass focused on the small manually identified areas, the entire vector field was swept using a much larger threshold. Velocity vectors with either component 1 m s^{-1} larger than the local mean were removed. This resulted in an average of 36,663 removed vectors for each canopy configuration (0.04% of total vectors in a given configuration). The PIV datasets generated during and/or analyzed during the current study are available from the corresponding author on reasonable request.

3 Results

Canopy flows can be divided into distinct vertical regions that can be used to characterize basic flow properties. From the ground surface to the top of the canopy ($zH^{-1} \lesssim 1$) is typically referred to as the CSL, an area that is characterized by low-velocity fluid and weak, intermittent, but complex, turbulence. Large vertical gradients occur at the top of the CSL ($zH^{-1} \approx 1$) as the result of the shear layer generated through mechanical shearing across the canopy top. Directly above the shear layer ($1 \lesssim zH^{-1} \lesssim 2$) is the roughness sublayer , a transition region where the fluid is influenced by both the slow moving fluid below and quick moving fluid above. Above the RSL is the atmospheric surface layer ($zH^{-1} \gtrsim 2$) where the fluid velocity profile generally follows Monin–Obukhov similarity theory. The primary goal of this study is to examine the spatial structure of turbulence in sparse, organized vegetative canopies with a focus on flow regions near the vegetation elements where significantly less data have been collected and where wind-tunnel measurements have the biggest advantage over field experiments. Analysis of the atmospheric surface layer is kept to a minimum due to lack of measurements in this region and the small canopy to boundary-layer height ratio in the wind-tunnel model, which suppresses the formation of a true logarithmic region in our study and many previous wind-tunnel canopy flow studies (e.g., Brunet et al. 1994; Böhm et al. 2013).

3.1 Mean Statistics

Before exploring the spatial characteristics of the flow, streamwise-averaged ensemble statistics are presented. This enables comparison to horizontally homogeneous canopies and is used to validate the wind-tunnel canopy model against atmospheric data collected within and above a sparse, organized canopy. The model canopy is compared to the normalized velocity statistics from vineyard canopy field measurements (Miller et al. 2017) for time periods when the flow is near-neutral thermal stratification and perpendicular to the vineyard-row direction. Field measurements were collected in the centre of a row in a vertical shoot positioning canopy of height 2.16 m and row spacing 2.5 m corresponding to a gap spacing of $1.15H$ and an LAI of 1. Streamwise-averaged velocity statistics have minimal deviation from ensemble-averaged values in the middle of the row where the Miller et al. (2017) tower

was located. An exception to this is the vertical velocity skewness for which the streamwise averaged value is lower than the middle row value, but for consistency the former is used for comparison.

Figure 2 presents the streamwise-averaged first through third ensemble velocity moments and the vertical Reynolds stress for all canopy configurations and compares it with the field data. Miller et al. (2017) error bars correspond to the ensemble standard deviation of the 30-min averaged field measurement values. Error bars for the $2H$ case correspond to the streamwise standard deviation of the ensemble statistics. The $\langle\overline{u}\rangle$ profiles (Fig. 2a) demonstrate that drag within the CSL produces an inflection point near the canopy top in all three test cases. The strength of this inflection can be characterized as inversely proportional to the normalized shear length scale $L_H H^{-1} = \langle\overline{u(H)}\rangle \left(\partial\langle\overline{u(H)}\rangle/\partial z\right)^{-1}$, which takes values of $L_H H^{-1} = 0.21$, 0.31, and 0.37 for the $1H$, $2H$, and $3H$ cases, respectively. All cases have a relatively strong inflection compared to previous canopy studies (Brunet 2020). This inflection creates a mixing-layer-like instability that generates large turbulent structures near the canopy top (Raupach et al. 1996) that are a primary driver of vertical momentum and scalar transport (Bailey and Stoll 2016). Below in the CSL, velocity profiles take on an exponential form where the influence of row spacing manifests as a shift of the profile to higher or lower velocities. While the Miller et al. (2017) data have a row spacing of $1.15H$, best agreement is not seen with the $1H$ case, but with the $2H$ case for $\langle\overline{u}\rangle$ and the $3H$ case

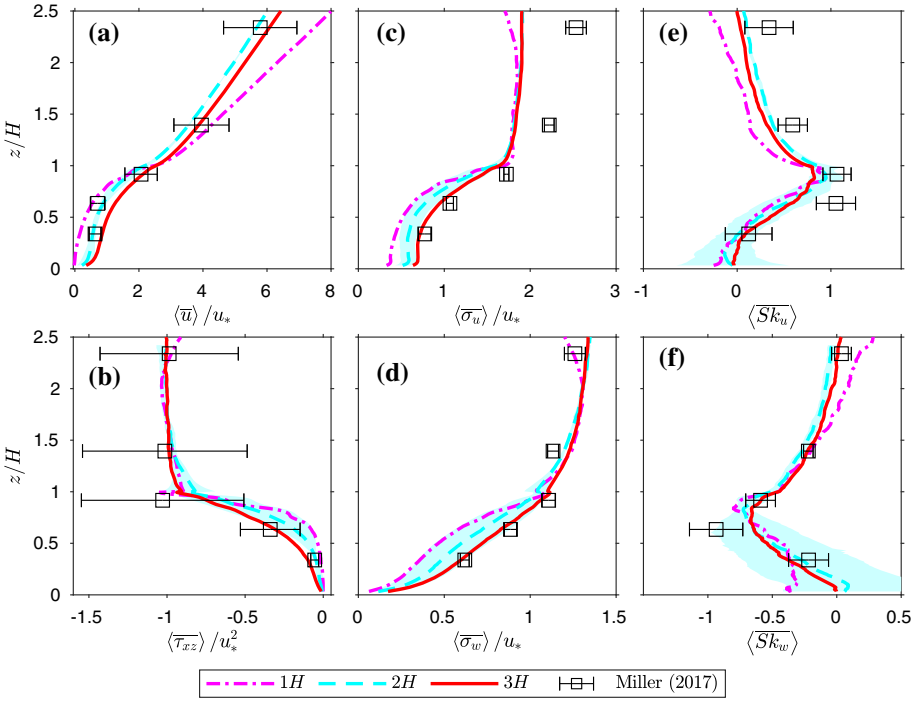

Fig. 2 Vertical profiles of streamwise-averaged ensemble statistics for the $1H$, $2H$, and $3H$ cases compared with the grape vineyard field data of Miller et al. (2017). Streamwise velocity **(a)**, Reynolds stress **(b)**, standard deviation of streamwise velocity **(c)**, and vertical velocity **(d)**, skewness of streamwise velocity **(e)**, and vertical velocity **(f)**. Shaded region indicates the streamwise standard deviation of the $2H$ ensemble statistics

for higher-order statistics. This is not entirely surprising since the horizontal structure of the canopy is not the only factor that affects streamwise-averaged ensemble statistics. Other considerations such as the LAI (a value of 1 for the field data, and $\approx$ 0.5–1.3 for the PIV data) and bulk boundary-layer flow conditions are expected to have an impact. The Reynolds stress ($\langle\overline{\tau_{xz}}\rangle = \langle\overline{u'w'}\rangle$, Fig. 2b) is nearly constant with height throughout the depth of the RSL for all cases, a common flow attribute above canopies (Harman et al. 2016; Brunet 2020). In the lower half of the CSL, $\langle\overline{\tau_{xz}}\rangle$ approaches zero and the vertical profile's curvature reduces as row spacing increases (LAI decreases) in general agreement with theory (Cionco 1972). Within the majority of the CSL, $\langle\overline{\sigma_u}\rangle = \langle\overline{u'u'}\rangle^{1/2}$ has a value approximately half its RSL value (Fig. 2). Trends in $\langle\overline{\sigma_u}\rangle$ are similar to $\langle\overline{u}\rangle$ with a marked increase with increasing row spacing in the CSL and a collapse above. The same cannot be said for $\langle\overline{\sigma_w}\rangle$ where the $3H$ case is nearly linear throughout the CSL, and as row spacing decreases the variance in the upper half of the CSL is reduced. Reynolds stress and velocity variances match the field data for the $3H$ case in the canopy, and all cases including the field data collapse above the canopy with one exception. In the RSL $\langle\overline{\sigma_u}\rangle$ is considerably underestimated in the wind tunnel, most likely due to the low background streamwise turbulence intensity (partly related to the small canopy to boundary-layer height ratio) compared to the atmosphere.

Higher-order moments of the velocity field are often associated with turbulent-flow structures and their vertical profiles exhibit distinct signatures in the CSL (Bailey and Stoll 2016; Brunet 2020). The standardized third velocity moment, the ensemble skewness, given by $\langle\overline{Sk_i}\rangle = \langle u_i'^3\rangle / \langle\overline{\sigma_{u_i}}\rangle^3$ is displayed in Fig. 2c, f. Within the canopy, where downward transport of high momentum fluid (sweeps) dominates, $\langle\overline{Sk_w}\rangle$ is negative, and $\langle\overline{Sk_u}\rangle$ is positive as expected. The basic shape of the vertical profiles of skewness also agrees with past measurements with peak negative (for $\langle\overline{Sk_w}\rangle$) and positive (for $\langle\overline{Sk_u}\rangle$) values just below the canopy top followed by a transition to near zero or small positive (negative) values above the surface (Brunet 2020). Above the canopy $\langle\overline{Sk_u}\rangle$ and $\langle\overline{Sk_w}\rangle$ compare well with the field data but the peak below the canopy top is underestimated in both cases.

Overall, agreement with the previous sparse, organized canopy field studies of Chahine et al. (2014) and Miller et al. (2017) and the large-eddy-simulation (LES) study of Bailey and Stoll (2013) are excellent for all statistics shown in Fig. 2, with the exception of an underestimation of the peaks in the streamwise and vertical skewnesses, which still fall within experimental error. Additionally, the values of the ensemble- and streamwise-averaged bulk statistics fall in the range of previous canopy flow studies (Finnigan 2000; Brunet 2020).

3.2 Mean Spatial Variability

Row spacing has an impact on not only streamwise-averaged statistics but importantly the spatial variability of turbulent processes in sparse, organized canopies. The open space in this canopy geometry gives the fluid enough unimpeded distance to create a distinct mix of horizontal and vertical variability.

To examine this spatial variability, we begin with the $\overline{u}$ velocity component within the canopy and its dependence on row spacing. The streamwise axis for ensemble-averaged plots has been normalized by the gap width $G = 1H, 2H$, and $3H$ for the $1H, 2H$, and $3H$ cases, respectively. Vertical profiles of the ensemble-averaged velocity are taken at $xG^{-1} = 0.25, 0.5$, and 0.75 for each canopy configuration and overlaid upon the two-dimensional distribution of $\overline{u}$ (Fig. 3). The $1H$ case profiles have less variation throughout the row gap than the $2H$ and $3H$ cases. For the $1H$ case, the distance the fluid travels before reaching the next row does not appear to be sufficient for the profile shape to significantly change. In contrast, in the $2H$

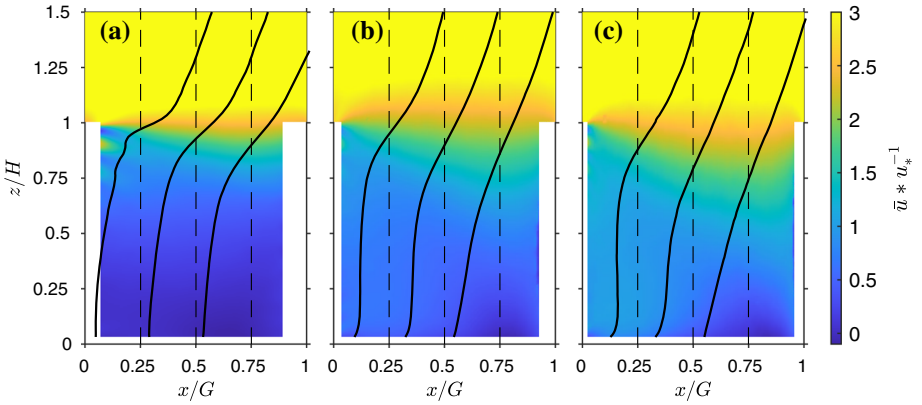

Fig. 3 Streamwise-vertical ensemble-averaged velocity distributions $\overline{u}\ u_*^{-1}$ for the $1H$ (**a**), $2H$ (**b**), and $3H$ (**c**) cases. Black lines indicate $\overline{u}\ u_*^{-1}$ profile shapes extracted along the vertical dashed lines located at xG^{-1} = 0.25, 0.5, and 0.75

and $3H$ cases the streamwise velocity profiles have appreciable streamwise variability. This emphasizes that gap normalization is inadequate to understand how a canopy will behave and that the physical wake recovery distance is likely a factor. In all cases, the flow through each canopy row is approximately uniform in the lowest two thirds of the canopy. This is a direct consequence of the chosen vertical structure and porosity of the rows. In windbreak studies it has been observed that when the optical porosity of a mesh is less than 55% a 'quiet' zone with a uniform velocity profile forms in the bleed flow just downstream of the windbreak. This does not seem to occur unless the upstream profile recovers from the exponential shape seen in the $1H$ case (Laws and Livesey 1978; Judd et al. 1996). As the fluid advects downstream from a row, surface friction acts to restore the boundary-layer profile. For individual windbreaks (elements of our model canopy) this recovery is well characterized for a variety of canopy densities and geometries (Judd et al. 1996; Maruyama 2008; Speckart and Pardyjak 2014). The streamwise velocity profiles in both the $2H$ and $3H$ cases follow the same general trends as windbreak recovery profiles where the inflection point is weakened as the flow transitions to a linear and then to logarithmic velocity profile.

Figure 4 displays the ensemble-averaged vertical momentum flux $\overline{\tau_{xz}}$. A downward flux of momentum is observed across the canopy top that remains relatively constant. This is a result of the blending of the high momentum fluid above the canopy into the uniform CSL profile. The process is dominated by the vertical turbulent mixing that occurs in conjunction with the growth in the downstream direction of a mixing layer that is initiated at the upstream row. Despite the considerable change observed in the velocity-profile shapes in the $2H$ and $3H$ cases, all have similar trends in the lower CSL where the turbulence is closer to isotropic and not dominated by this large downward flux of momentum. The transition between the significantly different upper and lower CSL $\overline{\tau_{xz}}$ values is not located at a fixed vertical location but follows a distinct linear trend downward. This trend is highlighted by solid black lines in Fig. 4 the location of which was chosen to best trace contours of constant $\overline{\tau_{xz}}u_*^{-2}$ in the transition region over the three canopy configurations. The mean $\overline{\tau_{xz}}u_*^{-2}$ value and the slope of the lines (S_τ) are presented in Table 2 along with the range that the lines were calculated over. The clear trend of increasing magnitude of S_τ with shorter gap width indicates that the presence of a downstream row alters the development of the mixing layer. Despite S_τ

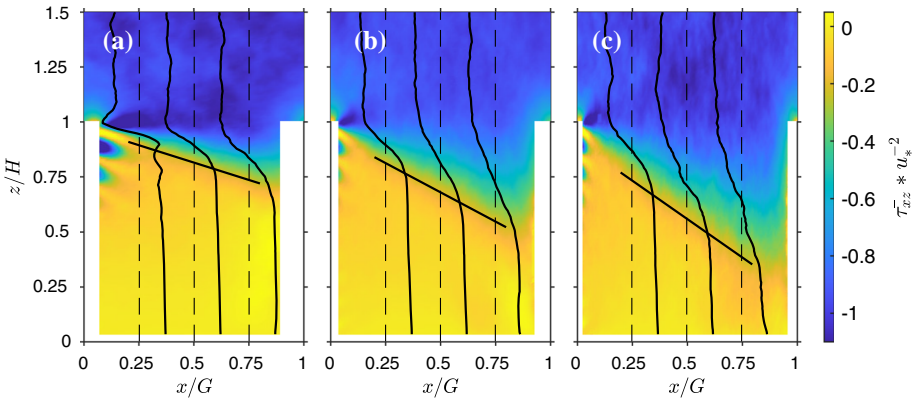

Fig. 4 Streamwise-vertical ensemble-averaged Reynolds stress distributions for the $1H$ (**a**), $2H$ (**b**), and $3H$ (**c**) cases. Black lines indicate $\overline{\tau_{xz}}\, u_*^{-2}$ profile shapes extracted along the vertical dashed lines located at xG^{-1} = 0.25, 0.5, and 0.75. Sloped black line indicates the transition from overlying RSL $\overline{\tau_{xz}}\, u_*^{-2}$ to near zero (S_τ)

Table 2 Slope and average values following contours of $\overline{\tau_{xz}}$ and $\overline{\omega_{xz}}$. Slope indicates the contour slope and mean value indicates the mean value extracted along this line over the given streamwise range

Slope Name	Slope	Mean Value	Range
S_τ^{1H}	−0.32	−0.20	$0.2 < xG^{-1} < 0.8$
S_τ^{2H}	−0.27	−0.21	$0.2 < xG^{-1} < 0.8$
S_τ^{3H}	−0.23	0.20	$0.2 < xG^{-1} < 0.8$
$S_{\omega 1}^{1H}$	−0.27	−0.29	10.8 mm $< x <$ 43.2 mm
$S_{\omega 1}^{2H}$	−0.1	−0.27	10.8 mm $< x <$ 43.2 mm
$S_{\omega 1}^{3H}$	−0.09	−0.28	10.8 mm $< x <$ 43.2 mm
$S_{\omega 2}^{1H}$	−0.43	−0.071	$0.3 < xG^{-1} < 0.6$
$S_{\omega 2}^{2H}$	−0.30	−0.073	$0.2 < xG^{-1} < 0.7$
$S_{\omega 2}^{3H}$	−0.23	−0.081	$0.2 < xG^{-1} < 0.7$

decreasing with increasing gap width, the $3H$ case ultimately penetrates farthest downward due to the larger downstream distance the unimpeded fluid can travel.

The ensemble-averaged in-plane vorticity $\overline{\omega_{xz}} = \overline{\frac{\partial w}{\partial x} - \frac{\partial u}{\partial z}}$ can also be used to visualize the spatially-developing mixing layer that originates at the upstream row canopy top and the quiet zone downstream of a row (Fig. 5). Three regions of varying horizontal and vertical extent can be observed in the $\overline{\omega_{xz}}$ distributions: a high magnitude region originating from the top of the canopy row (region 1), a descending region with a magnitude that approaches the values in the RSL above (region 2), and a region with near zero vorticity in the quiet zone just downstream of the upstream row (region 3). The lines delineating these three regions were explored using the same method as for $\overline{\tau_{xz}}$ (Fig. 4) in Fig. 5 and quantified by calculating the slope of the lines ($S_{\omega 1}$ and $S_{\omega 2}$ in Table 2). Region 1 spans a fixed physical distance, therefore $S_{\omega 1}$ is calculated over a small constant area near the upstream row's canopy top. To help visualize the size and slopes displayed in this figure, the same information with an x axis scaled by H is provided as supplementary information (Online Resource 1). The development

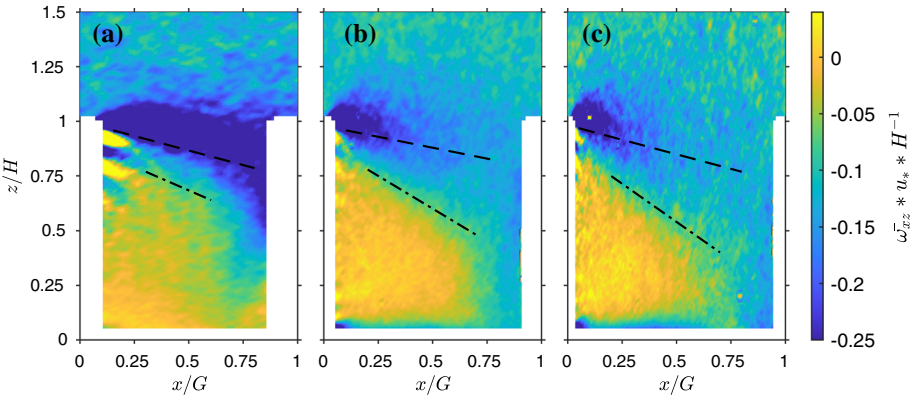

Fig. 5 Streamwise-vertical ensemble-averaged vorticity distributions $\overline{\omega_{xz}} u_* H^{-1}$ for the $1H$ (**a**), $2H$ (**b**), and $3H$ (**c**) cases. Dashed line indicates downward slope of highly turbulent mixing generated at the canopy top ($S_{\omega 1}$). Dash–dotted line indicates slope of blending between the mixing zone and quiet zone ($S_{\omega 2}$)

of region 1 (above the $S_{\omega 1}$ line) follows the highly turbulent spatially-developing mixing layer at the canopy top. For the $1H$ case this region spans across the entire canopy gap creating a horizontally constant layer, while the larger gap width cases reveal a breakdown of high magnitude vorticity in the downstream direction and the effective blending of this region with the surface layer. For the $2H$ case this occurs at $xG^{-1} \approx 0.5$ and in the $3H$ case at $xG^{-1} \approx 0.25$. For the $3H$ case the breakdown is nearly complete and $\overline{\omega_{xz}}$ reverts fully to its value observed in the surface layer before reaching the downstream row. Below the $S_{\omega 1}$ line, a descending transition occurs from the highly turbulent mixing in region 1 to region 2. For the larger row-spacing cases, $S_{\omega 1}^{2H}$ and $S_{\omega 1}^{3H}$ have similar values indicating that this feature has little dependence on row spacing. In the $1H$ case the high-vorticity region hits the downstream row before dissipating which pushes all this highly turbulent fluid downward, leading to a larger $S_{\omega 1}^{1H}$ value. In the lower CSL, region 2 blends into region 3 along $S_{\omega 2}$ (dash-dotted line Fig. 5) producing an increase of $\overline{\omega_{xz}}$ in the downstream direction. In a similar fashion to the shear stress (Fig. 4), the xG^{-1} distance at which this occurs shifts towards the ground as xG^{-1} increases. The slope $S_{\omega 2}$ follows a trend very similar to that of S_τ with the magnitude increasing as row spacing is reduced. Although not as linear as S_τ, this suggests that the downward transport of momentum is linked to the blending of these two regions, but due to the arbitrary thresholds chosen between zones it is difficult to compare directly between different statistical quantities.

The overall structure of the mean flow through the model canopy can be summarized using the ensemble-averaged streamlines and vertical velocity $\overline{w}$ (Fig. 6). As with Fig. 5, in order to help conceptualize sizes of flow features, Fig. 6 has been plotted with physical distances and an x axis of xH^{-1} and added as supplementary information (Online Resource 2). Inside the canopy a region of positive vertical velocity is observed that extends downward from the top edge of the upstream row following the development of the streamwise velocity profiles (Fig. 3) and the blending of high and low $\overline{\omega_{xz}}$ fluid (dash–dotted black line $S_{\omega 2}$). Above this region mean vertical advection is small and instead downward turbulent momentum flux (Fig. 4) and vorticity (Fig. 5) dominate. Suppression of mixing-layer growth is again observed as it comes in contact with a zone of strong negative vertical velocity located directly upstream of the downstream row (Fig. 5). This zone has similar properties to the upwind cavity observed in street canyons and has been observed in the shear-layer regime cases of Hamed et al.

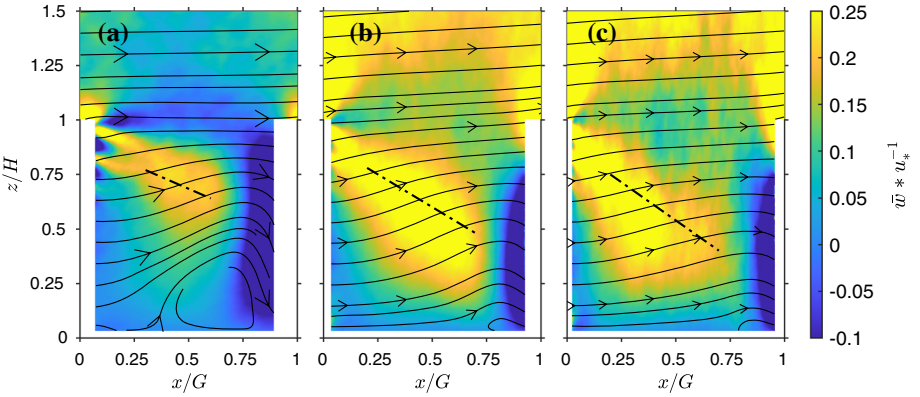

Fig. 6 Ensemble-averaged streamlines overlaid on the vertical velocity component ($\bar{w}u_*^{-1}$) for the $1H$ (**a**), $2H$ (**b**), and $3H$ (**c**) cases. The dash-dotted line corresponding to $S_{\omega 2}$ has also been included

(2020), indicating its presence is possibly tied to the interaction of the growing mixing layer with a downstream canopy element (Addepalli and Pardyjak 2013). The horizontal extent of this zone is approximately constant for the three cases indicating that for sufficiently spaced rows it is most likely to be a function of canopy density and the incoming velocity magnitude. In the $1H$ case, the zone expands vertically from its value of $\approx 0.75zH^{-1}$ for the $2H$ and $3H$ cases to nearly $0.9zH^{-1}$ indicating that the disruption of the upstream row originating mixing layer in the $1H$ case also has some impact on this region of persistent negative $\bar{w}$.

The homogeneity of the streamwise velocity profiles observed in Fig. 3 for the $1H$ case does not translate to the ensemble-averaged streamlines and vertical-velocity patterns. Here we see a significant recirculation zone that forms in conjunction with the negative $\bar{w}$ zone flow. Since the blockage is strong enough relative to the streamwise velocity, the fluid cannot fully be pushed through the canopy flow and a vortex is formed. A singular vortex is observed in the recirculation zone of all three cases with the relative size growing as row spacing decreases.

3.3 Turbulence Kinetic Energy

The ensemble-averaged total in-plane TKE defined as $\overline{e} = \frac{1}{2}\left[\overline{(u')^2} + \overline{(w')^2}\right]$ is presented in Fig. 7. Two important regions are observed in the CSL. First is the relatively weak TKE generated in the bleed flow directly behind each canopy row. Work done on the mean flow by the canopy elements converts mean kinetic energy (MKE) into TKE at the wake scale of the canopy elements (i.e., mesh spacing here), a process referred to as the spectral short cut (Finnigan 2000). Bleed-flow turbulence quickly decays downstream of the row and the main source of TKE comes from the highly turbulent RSL above. Both regions of TKE generation are persistent throughout all canopy configurations with increased penetration of high-magnitude TKE from the RSL correlated to increased G values. In the downstream half of the canopy $\overline{e}$ is dominated by the downward flux of momentum and has a nearly identical trend to $\overline{\tau_{xz}}$ (Fig. 4). Turbulence-kinetic-energy distributions in windbreak flow show similar patterns to our model canopy (Patton et al. 1998). The slight downward curve observed in $\overline{e}$ contours for windbreak flows is present in the downstream half of our model canopy, but is not as pronounced. Despite the slight change in distribution both the windbreak

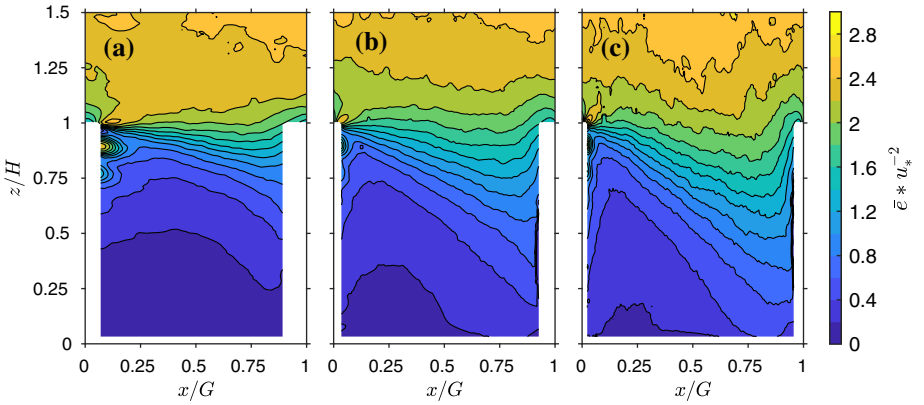

Fig. 7 Contours of ensemble-averaged in plane TKE ($\overline{e}u_*^{-2}$) for the $1H$ (**a**), $2H$ (**b**), and $3H$ (**c**) cases

and $3H$ case experience downward penetration of TKE to approximately $zH^{-1} = 0.25$ at $xH^{-1} = 3$. As row spacing decreases, a shift away from the curved windbreak profile to more linear contours, which mimic the shear layer, is observed. The in-plane TKE within the canopy gap of Hamed et al. (2020) had similar curvature and contour shapes but with a much steeper descent and downward penetration of TKE all the way to the surface near $xH^{-1} = 2$. The individual variance components (not shown) that contribute to in-plane TKE were also explored. The ensemble-averaged streamwise velocity variance $\overline{u'^2}$ closely follows the trends of $\overline{e}$ with distinct bleed flow and upstream recirculation zones whose extents are gap-width dependent. The ensemble-averaged vertical-velocity variance $\overline{w'^2}$ has a closer to linear trend (e.g., contours remain equally spaced) until it reaches the zone of strong negative $\bar{w}$ with a magnitude approximately half that of $\overline{u'^2}$.

3.3.1 Budget Analysis Framework

Understanding the physical processes that govern the generation of turbulent fluctuations can be done through an exploration of the TKE transport equation. Figure 7 demonstrated that significant TKE penetrates into the canopy, but the physical mechanisms associated with this have not been identified. Above the canopy and in between the rows, the Reynolds-averaged TKE budget equation is given by

$$\underbrace{\overline{u_i}\frac{\partial \overline{e}}{\partial x_i}}_{\text{I}} = \underbrace{-\overline{u_i' u_j'}\frac{\partial \overline{u_i}}{\partial x_j}}_{\text{II}} \underbrace{-0.5\frac{\partial}{\partial x_i}[\overline{u_i' u_j' u_j'}]}_{\text{III}} \underbrace{-\ \overline{\epsilon}}_{\text{IV}} \underbrace{-\ \Re}_{\text{VII}}, \tag{1}$$

where term I represents the advection ($\overline{A}$), II the mechanical shear production ($\overline{P_s}$), III the turbulent transport ($\overline{T_t}$), and IV the viscous dissipation ($\overline{\epsilon}$) of TKE (Stull 1988). Term VII ($\Re$) is a residual term that includes the local unsteady change or storage of TKE, pressure correlation, molecular transport, and buoyancy terms which were not measured during the experiments. While the pressure term is expected to be a large TKE sink, molecular transport and buoyancy effects are likely negligible due to the high Reynolds number and near-neutral thermal conditions inside the wind tunnel.

In canopy flow it is common to apply a volume-averaging operator to Eq. 1 across a thin horizontal slice (in this case G wide and a vector pitch = 0.7 mm tall) that preserves vertical flow properties and excludes canopy material eliminating plant-scale horizontal heterogeneity and generating a singular representative budget of a plant canopy (Raupach and Shaw 1982; Brunet 2020). Expanding the general form of the volume-averaged budget and assuming a constant freestream velocity plus moving terms that involve unavailable out-of-plane gradients and velocities to the residual leads to the final form of the volume-averaging in-plane TKE budget

$$0 = \underbrace{\left(\langle\overline{u'w'}\rangle\frac{\partial\langle\overline{u}\rangle}{\partial z} + \langle\overline{w'w'}\rangle\frac{\partial\langle\overline{w}\rangle}{\partial z}\right)}_{\text{II}} + \underbrace{0.5\left(\frac{\partial\langle\overline{u'u'w'}\rangle}{\partial z} + \frac{\partial\langle\overline{w'w'w'}\rangle}{\partial z}\right)}_{\text{III}} + \underbrace{\langle\overline{\epsilon}\rangle}_{\text{IV}} + \underbrace{0.5\left(\frac{\partial\langle\overline{u'u'}''\overline{w}''\rangle}{\partial z} + \frac{\partial\langle\overline{w'w'}''\overline{w}''\rangle}{\partial z}\right)}_{\text{V}} - \underbrace{\left(\langle\overline{u'w'}''\frac{\partial\overline{u}}{\partial z}\rangle + \langle\overline{w'w'}''\frac{\partial\overline{w}}{\partial z}\rangle\right)}_{\text{VI}} + \underbrace{\langle\Re\rangle}_{\text{VII}}, \tag{2}$$

where terms II–IV and VII are the volume-averaged equivalents of the same terms in Eq. 1 specifically, $\langle\overline{P_s}\rangle$,$\langle\overline{T_t}\rangle$, $\langle\overline{\epsilon}\rangle$, and $\langle\Re\rangle$, respectively. The non-commutative properties of the Reynolds-averaging and volume-averaging operators generate two additional terms in Eq. 2 that represent the impact of unresolved horizontal plant-scale turbulence: the dispersive transport (T_d) and wake production (P_w) (V and VI). Calculation of all terms in Eq. 2 using the PIV data is straightforward with the exception of the dissipation rate ($\overline{\epsilon}$). The TKE dissipation rate is often calculated in canopy flow using the slope of streamwise velocity spectra (E_{uu}) in the inertial subrange (Brunet et al. 1994; Van Hout et al. 2007; Yue et al. 2008; Christen et al. 2009). Due to the horizontal complexity of the canopy it is more practical to estimate $\overline{\epsilon}$ using the second-order streamwise spatial structure function and Kolmogorov's two-thirds law (Miller and Beresh 2021). The streamwise-structure function is defined as $S_{uu}(r, x, z, n) = [u(x + r, z, n) - u(x, z, n)]^2$ where r is the separation distance. The function S_{uu} is evaluated for all locations (x, z) and instantaneous velocity fields (n) and then the dissipation was estimated as

$$\overline{\epsilon(x, z)} = \left\langle\left\langle\frac{\overline{S_{uu}(r)}^{3/2}}{C^{3/2}r}\right\rangle\right\rangle, \tag{3}$$

where the subset of r used was identified to be within the inertial subrange, C is a universal Kolmogorov scaling constant (taken as 2.0, Pope 2000), and $\langle\langle\ \rangle\rangle$ denotes an average over all separation scales within the inertial subrange. The determination of what r corresponds with the inertial subrange was done by plotting the autocorrelation function and determining the average transition from a linear to nonlinear relation according to Pope (2000). A uniform range of 13.8 mm $< r <$ 23.9 mm was used for consistency between canopy spacings and heights. Results had minimal sensitivity to both the upper and lower boundaries of r. Example structure functions for each canopy spacing at different xG^{-1} locations can be found in the supplementary information (Online Resource 3).

3.3.2 Volume-Averaged Budgets

The main source of TKE in the upper CSL and RSL comes from shear production, which is created as MKE is broken up by the large vertical gradients across the canopy top. The peak of

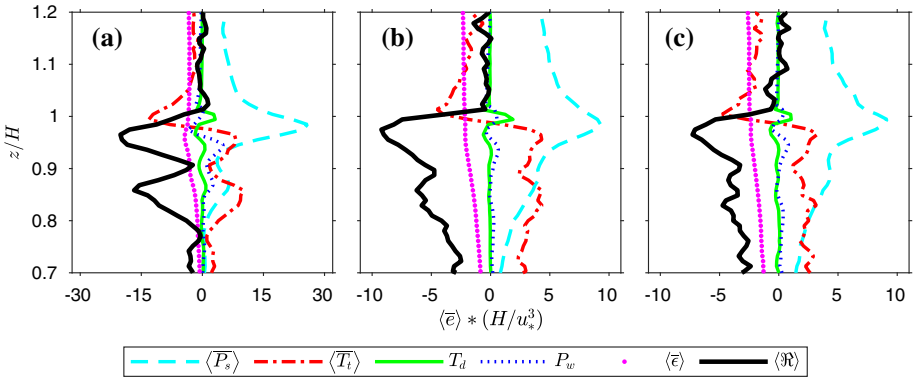

Fig. 8 Ensemble- and volume averaged TKE budget for the $1H$ (**a**), $2H$ (**b**), and $3H$ (**c**) cases. $\langle\overline{P_s}\rangle$ is the shear production, $\langle\overline{T_t}\rangle$ the turbulent transport, T_d the dispersive transport, P_w the wake production, $\langle\overline{\epsilon}\rangle$ the dissipation, and $\Re$ the residual of TKE

$\langle\overline{P_s}\rangle$ (Eq. 2) is slightly below the canopy top for all cases, but the $1H$ case sees almost double the magnitude of the $2H$ and $3H$ cases (Fig. 8). The distinct edge at the top of the model canopy creates such large vertical gradients in the flow field that $\langle\overline{P_s}\rangle$ is enhanced to almost double the levels seen in atmospheric canopies (for the $2H$ and $3H$ cases), but is comparable to structured laboratory and LES studies (Yue et al. 2008; Christen et al. 2009; Nebenführ and Davidson 2015; Miller et al. 2017). In the RSL where the stress profile is constant (Fig. 4), $\langle\overline{P_s}\rangle$ trends toward a constant value as expected and is balanced by loss of TKE through $\langle\overline{T_t}\rangle$ and eventually $\langle\overline{\epsilon}\rangle$. A transition in $\langle\overline{T_t}\rangle$ from a sink of TKE (negative sign) above the canopy to a source (positive sign) just below the canopy top occurs through processes associated with the mixing layer. Farther downward into the CSL $\langle\overline{P_s}\rangle$ trends toward zero with $\langle\overline{T_t}\rangle$ following, but at a slower rate, making it the dominant source of TKE at $\approx 0.85H$ for all three canopy configurations. In other studies the $\langle\overline{T_t}\rangle$ maximum occurs around $0.75H$ (Yue et al. 2008; Miller et al. 2017); this discrepancy will be explored further in the next section.

The two terms specific to volume-averaged budgets, P_w and T_d, have much smaller magnitudes compared to $\langle\overline{P_s}\rangle$ and $\langle\overline{T_t}\rangle$ but non-zero contributions to the total TKE for $0.85 < zH^{-1} < 1$. The wake production P_w has been reported as a very significant source of TKE near the canopy top, typically of the same order of magnitude as $\langle\overline{P_s}\rangle$ (Brunet et al. 1994; Böhm et al. 2013; Miller et al. 2017). These studies report a modelled form of this term from Raupach and Shaw (1982), the direct calculation used here is significantly lower. We suspect that unresolved contributions to this term may be large due to the spanwise nature of turbulent structures that play a significant role in canopy flows (Bailey and Stoll 2016). Another possibility is that the approximate form used in prior studies is not valid for all complex canopy configurations. Further research that measures both vertical and horizontal planes of data would be required to make a conclusive statement. The dispersive transport T_d shows a small contribution near the canopy top. The peak corresponds to the sign change observed in $\langle\overline{T_t}\rangle$.

Observed trends in all TKE components continue into the lower canopy without significant alteration (not shown). This includes $\langle\overline{P_s}\rangle$, which in the lower half of the canopy is near zero with little contribution to TKE production from either the shear layer above or the ground surface. All canopy configurations have similar trends, even the $3H$ case where higher velocity fluid penetrates closer to the surface. The only remaining source of TKE in

the lower half of the CSL is $\langle \overline{T_t} \rangle$, where the TKE is then lost to $\langle \overline{\epsilon} \rangle$ and the residual (most likely dominated by pressure transport) in equal amounts.

3.3.3 Reynolds-Averaged Budget Terms

Exploring the two-dimensional spatial distributions of the Reynolds-averaged budget terms including $\overline{A}$, $\overline{P_s}$, $\overline{T_t}$, $\overline{\epsilon}$, and $\overline{\Re}$ from Eq. 1 can provide context to the observed trends in the volume-averaged budget (Fig. 9). Slope lines using the S_τ (Fig. 9d–i, m–l), $S_{\omega 1}$ (Fig. 9a–i), and $S_{\omega 2}$ (Fig. 9d, e, f) values given in Table 2 have been overlayed on the TKE terms they are most connected to. Spatial distributions (excluding ϵ which due to the nature of its calculation is already filtered) have been low-pass filtered with a spatial convolution filter of scale $\Delta = 7.5$ mm to provide visual clarity.

For all cases, $\overline{P_s}$ shows a large spike in TKE generation originating at the top of the upstream row (Fig. 9a, b, c). Downstream of the leading edge, $\overline{P_s}$ quickly propagates into the fast moving fluid above becoming the main source of TKE in the RSL. Approximately $1H$ downstream from the upstream row the inflection in the average streamwise velocity profile weakens (Fig. 3). This produces a near uniform $\overline{P_s}$ for the $1H$ case while the $2H$ and $3H$ cases have a constant decrease with downstream distance after this transition. The shear in

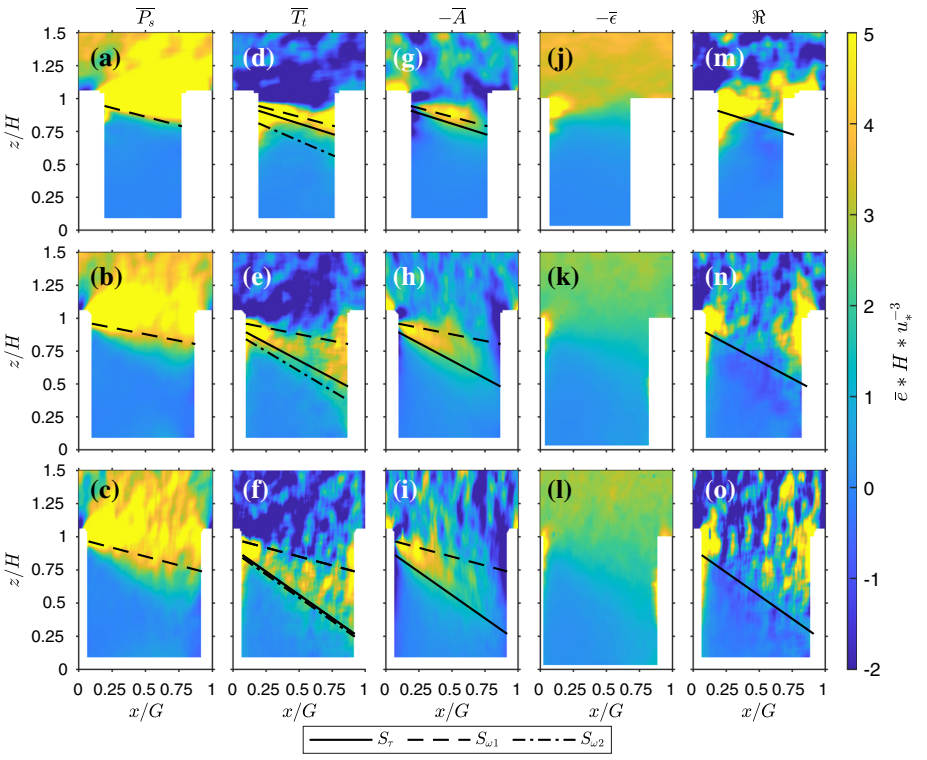

Fig. 9 Ensemble-averaged two-dimensional TKE budget distributions for $1H$ (a, d, g, j, m) $2H$ (b, e, h, k, n) and $3H$ (c, f, i, l, o) cases. Terms from the left to right: shear production of TKE $\langle \overline{P_s} \rangle$ (a, b, c), turbulent transport of TKE $\langle \overline{T_t} \rangle$ (d, e, f), advection of TKE $\langle \overline{A} \rangle$ (g, h, i), dissipation of TKE $\langle \overline{\epsilon} \rangle$ (j, k, l), and residual $\Re$ (m, n, o). Lines indicate slopes S_τ, $S_{\omega 1}$, and $S_{\omega 2}$ given in Table 2

this region behaves similarly to urban canopies, which observe a decline in $\overline{P_s}$ across the top of a building (Giometto et al. 2016; Blackman et al. 2017). The decrease in centreline $\overline{P_s}$ follows the pattern observed in $\overline{\omega_{xz}}$ across the canopy top. The overlayed $S_{\omega 1}$ in Fig. 9a, b, c directly coincides with the bottom edge of the large source of $\overline{P_s}$, a strong indication that growth of the mixing layer originating at the upstream row is connected to a significant portion of the production of shear at the canopy top. Below $S_{\omega 1}$ the $2H$ and $3H$ cases observe additional shear generated in conjunction with the developing velocity profiles.

The sign change of $\langle\overline{T_t}\rangle$ observed in Fig. 8 is also observed in $\overline{T_t}$ (Fig. 9d, e, f). The vertical location where this transition occurs lowers with downstream distance through the canopy row gap. The peak $\overline{T_t}$ value occurs directly below the descending transition explaining the lack of a true maximum in Fig. 8. Giometto et al. (2016) also observed this trend in the wake of their sparse building array, but Blackman et al. (2017) less so due to the tight arrangement of blocks. The slope line $S_{\omega 1}$ is again shown and clearly coincides with the slope of the sign change in $\overline{T_t}$ for the $2H$ and $3H$ cases. This indicates that TKE is not generated from MKE throughout the entirety of the mixing layer but that locally in this upper portion TKE generation is related to turbulent mixing and shear processes. Below S_τ, $S_{\omega 1}$ and $S_{\omega 2}$ are also shown and appear to follow the transition of $\overline{T_t}$ to zero. The similarity of these slopes lead us to believe that when it has space to grow, the shear layer's downward penetration is mostly due to the downward flux of momentum, which is also tied to the turbulent transport of TKE. The region in between $S_{\omega 1}$ and $S_{\omega 2}$ corresponds to the lower mixing layer where the dominant turbulent processes are attributed to transport and not shear. While observed trends for $S_{\omega 1}$ connecting to $\overline{P_s}$ hold between the $2H$ and $3H$ configurations, a breakdown is observed in the $1H$ case. In this case the sign change remains at a relatively constant position following the consistent horizontal nature of the canopy-top mixing observed in $\overline{\omega_{xz}}$ (Fig. 5) whereas $S_{\omega 1}$ protrudes down into the CSL. Below the canopy top S_τ appears to maintain a similar slope to $\overline{T_t}$ in the downstream half of the canopy, but $S_{\omega 2}$ is much steeper and mixing in the $1H$ case is most likely attributed to another process.

Advection plays an important but localized role in balancing the TKE generated by $\overline{P_s}$ and $\overline{T_t}$ (Fig. 9g, h, i). The region of TKE generation by $\overline{T_t}$ is balanced by $\overline{A}$ acting as a sink of TKE. Contributions from $\overline{A}$ seem to diminish at the same downstream point related to $S_{\omega 1}$. Blackman et al. (2017) observes a transition from sink to source near the downstream centre of the canopy. While this trend is observed in all three canopy configurations, the transition happens very near the downstream row for the $1H$ case. Trends in $\overline{\epsilon}$ closely follow that of $\overline{e}$ (Fig. 7) acting as a proportionally equal sink of TKE regardless of the source (Fig. 9j, k, l). The residual $\overline{\Re}$ is high at the origination of the canopy top spatially-developing mixing layer and follows the descent of S_τ into the CSL (Fig. 9m, n, o). The upper edge of its extent is not bounded by $S_{\omega 2}$ differing from both $\overline{T_t}$ and $\overline{A}$. Near the middle of the mixing layer $\overline{\Re}$ is relatively minimal compared to the two regions located near the top of the upstream and downstream canopy rows. For the $1H$ case a horizontal homogeneous region is formed across the canopy top. We suspect that in these near-row regions the largest contribution to $\overline{\Re}$ is from the unknown pressure term. Another likely contribution is from the spanwise velocity and gradients near the canopy top (Bailey and Stoll 2016). In the quiet zone $\overline{\Re}$ is near zero, and as expected TKE generated by $\overline{T_t}$ is well balanced by $\overline{\epsilon}$.

4 Conceptual Model of the Flow Structure

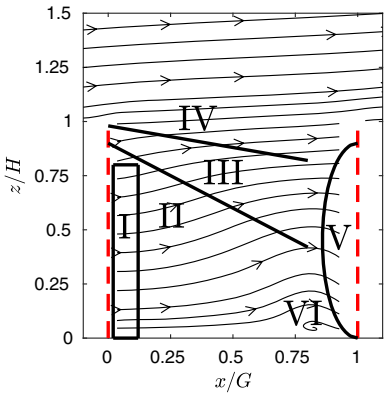

Fig. 10 Conceptual model of mean and turbulent processes of flow through sparse, organized canopies. Zone I is the bleed flow, II the quiet zone, III the shear-mixing zone, IV the transport-mixing zone, V the pressure zone, and VI the recirculation zone

The observations from the previous sections can be synthesized into a compact conceptual model that summarizes the mean and turbulent processes that govern transport in sparse, organized canopies. The conceptual model represents the fully developed flow (i.e., no canopy entrance or exit effects) through a single canopy gap beginning at the gap's upstream row. Contact with canopy elements disturbs the flow generating distinct spatial regions marked I–VI (Fig. 10). The bleed flow (I) is characterized by a significant reduction in overall fluid momentum as work is done on the fluid by the canopy elements. In this region, the streamwise velocity profile generated in the canopy wake is dependent on both its upstream shape as well as the row porosity. Small-scale turbulence dominates this zone as MKE is broken down and converted into TKE at the spatial scale of the canopy elements (Fig. 7). With downstream distance, structures broken up by the canopy elements combine, resulting in a steady increase of TKE through the bleed-flow region. After this increase in TKE, the flow transitions to the next region, the quiet zone (II). The quiet zone behaves similarly to the lower portion of a homogeneous canopy's CSL consisting of weak fine-scale isotropic turbulence and minimal mixing (Fig. 5) with TKE levels decaying in the streamwise direction (Fig. 9). Despite similar flow characteristics, departure from homogeneous canopy flow is observed through the addition of mean upward flow patterns (Fig. 6) throughout the CSL. In the upper CSL fluid not only bleeds through the canopy but is sheared off the top edge forming a spatial and temporal mixing layer (regions III and IV). The Raupach et al. (1996) mixing-layer analogy compares the instability generated by the streamwise velocity profile's inflection point (Fig. 3) to that of a plane mixing layer where high- and low-fluid momentum are vertically mixed producing an instability in the flow. This is further augmented by the growing spatial mixing zone that originates at the top of the upstream row. This feature is similar to that observed in windbreak flows that leads to a complex mix of physical processes that include turbulent mixing, momentum transport, and large sources of TKE production (Judd et al. 1996). The bulk of turbulence produced in the mixing layer is located in the shear-mixing zone (IV) where shear processes act to mix the fluid over a set streamwise distance (Figs. 5 and 9a–c). While shear is generated in zone IV, it persists well into the lower mixing layer (Fig. 4) alongside significant turbulent mixing. In this area, the transport-mixing zone (III), shear and turbulent energy are mainly a result of turbulent transport process (Fig. 9d–f). Further growth of both mixing-layer regions is eventually impeded by the pressure zone (region V), which forms as the fluid builds up and is diverted as a result of form drag from the downstream row. Effects of this zone are unique to row oriented canopies as homogeneous canopies either have elements that are too tightly packed for this zone to develop or are composed of more

three-dimensional objects enabling flow to divert horizontally, which minimizes the build up (Böhm et al. 2013). This feature is likely present in windbreak flows, but windbreak flow studies are typically focused on the downstream effects of the windbreak and therefore include minimal discussion (e.g., Speckart and Pardyjak 2014). In the lower CSL the quiet zone is also impeded by the high-pressure region. Flow blockage appears to have little influence on turbulence in this region but is responsible for the mean upward flow patterns seen in zone II. As the blockage becomes severe enough (canopy drag force exceeds inertia), the fluid is unable to fully break through the canopy elements and diverts downward curling backwards into the recirculation zone (VI). Despite not being as pronounced as when fluid connects with bluff objects (Addepalli and Pardyjak 2013; Hayati et al. 2019), this zone appears to be a persistent features in this canopy architecture.

Row spacing and canopy density are both important parameters that determine how critical a role each zone plays in the overall dynamics of sparse, organized canopies. As row spacing decreases the higher overall canopy density leads to an increase in drag and reduced streamwise velocity throughout the CSL. This accentuates some of the mean flow patterns including the upward flow (zone II) and recirculation (zone VI). Recovery of the streamwise velocity profile is reduced as the mixing layer (zones III and IV) does not penetrate into the CSL, resulting in vertical profiles of the streamwise velocity being relatively constant throughout the canopy. The strong inflection in the profile at the canopy top creates vigorous but highly localized production of shear directly across the canopy top. Attenuation of the vertical growth of both zones III and IV occurs producing a horizontally homogeneous shear and transport layer in the vicinity of the canopy top. These thin layers still act to generate and transport turbulent energy down into the canopy, but their extent is severely limited and the CSL is primarily dominated by the quiet zone. Overall, small row gaps behave similarly to homogeneous canopies with the exception of a larger than normal shear production located at the canopy top produced by the structured top edge of the canopy row and the presence of zones V and VI as a result of the continuous spanwise structure of the canopy. Interestingly, for small row gaps, the presence of zones V and VI appears to have a greater impact on mean flow patterns than turbulence levels. As the canopy gap increases the streamwise velocity profile begins to recover towards a boundary-layer-like shape somewhere between linear and logarithmic. The shape it reaches by zone V along with the row porosity determines the shape of the bleed flow profile. The mixing zones, III and IV, both see increased vertical growth with downstream distance following patterns observed in windbreak flow (Judd et al. 1996). Increases in the size of these zones allows significant vertical mixing to be present much lower into the CSL. What attenuation we do see of the mixing layer by contact with zone V occurs in zone IV where vertical transport is impeded. This is clearly indicated in Table 2 where both S_τ and $S_{\omega 2}$ see a trend of decreasing slope with increasing gap width. Mixing in zone III begins to dissipate around $xH^{-1} = 1.5$ and while shear production is still present, $S_{\omega 1}^{2H}$ and $S_{\omega 1}^{3H}$ show almost identical slopes indicating contact with zone V has no affect on this region past this physical downstream distance. Growth of region IV slowly encompasses the quiet zone to become the dominant feature of the interior CSL towards the downstream end of the gap. This process behaves similarly to that of windbreak flows where the mixing zone begins to eventually fully encompasses the quiet zone (Judd et al. 1996).

5 Summary

Turbulence in sparse, organized canopies was explored using a model vineyard canopy placed inside a wind tunnel. Particle image velocimetry measurements of streamwise and vertical velocity components were taken in the streamwise-vertical plane along the centreline of a single row gap. The dependence of mean and turbulent flow statistics on row spacing was explored by varying the gap width between canopy rows. Streamwise-averaged mean horizontal velocity, standard deviations of the streamwise and vertical velocity components, and the skewness of the streamwise and vertical velocity components from the wind-tunnel experiment all have good agreement with the vineyard field measurements of Miller et al. (2017).

Ensemble-averaged statistics display not only the vertical variation commonly observed in canopies but significant streamwise variation in mean and turbulence processes within the canopy row gaps. Mean trends observed through streamlines of the flow include a region of upward flow in the centre of the canopy followed by a downward flow and recirculation zone just upstream the downstream row. The upward flow is produced as the streamwise velocity profile develops alongside the blending of high and low turbulence fluid associated with the bottom edge of the spatially developing mixing layer at the canopy top. The downstream row's blockage is responsible for pushing the fluid downward and eventually recirculating the fluid. The downward-flow region remains approximately constant between all three cases while the upward flow and recirculation become less prominent as the streamwise velocity inside the canopy increases. Streamwise variation of turbulence is dominated by the growing spatial mixing layer originating from the top edge of the upstream row. Turbulence associated with this mixing layer was observed in the ensemble-averaged stress, vorticity, and total in-plane TKE distributions. Three slope lines following contours of areas of interest in the stress and vorticity were calculated. The slope of the lines corresponding to the blending of the mixing layer with the quiet zone below reduced as row spacing increased. The slope line corresponding to the large area of mixing near the canopy top and directly downstream where the mixing layer originates remained constant for the two wider row-spacing cases where this feature was given space to naturally dissipate but saw a sharp increase in the narrowest case when the feature remained constant throughout the canopy.

Understanding the nature of CSL turbulence was achieved through an in-depth analysis of the flow's TKE budget. Traditional volume-averaged TKE budgets, often used in canopy flow, were presented alongside Reynolds-averged budgets to assess the most active processes in each area of the CSL. Volume-averaged budgets followed similar trends to past canopy flow studies where strong shear production and a transition from source to sink of turbulent transport were observed at the canopy top. Lower into the canopy, shear production begins to slowly become less important and turbulent transport takes over becoming the dominant source of TKE near the upper third of the CSL. In this region the maximum often observed in the turbulent transport term was not observed as the Reynolds-averaged distributions showed that the vertical maximum moves downward with downstream distance. In-plane contributions from the wake production and turbulent transport terms exclusive to volume-averaged budgets were only found to significantly contribute to the budget just below the canopy top with magnitudes lower than reported in prior studies. Spatial distributions of terms in the Reynolds-averaged budget were presented showing that shear production is contained to near the canopy top and heavily connected to the large mixing observed in the vorticity distribution. Turbulent transport's peak is observed to follow the mixing layer's descent into the canopy with the sign transition following the slope of the large mixing region. Below

farther into the CSL, turbulent transport transitions to zero following the bottom edge of the mixing layer.

The key mean and turbulent features were then condensed into a conceptual model that describes sparse-organized canopy flow in an intuitive way. The model is built up from six distinct flow regions: the bleed flow, quiet zone, shear mixing and transport mixing layers, pressure zone, and recirculation zone. The bleed flow containing low-momentum fluid and TKE generated through the breakdown of MKE by the canopy elements transitions into the quiet zone's uniform flow and decaying isotropic turbulence. Above, the mixing layers make up the bulk of turbulence penetrating into the canopy with shear production and turbulent transport acting as the two main mechanisms. The downstream row's blockage is observed through the pressure zone associated with downward movement of the flow and eventual backflow found in the recirculation zone.

Future work is required to expand the conceptual model to the conditions observed in real world canopies. Atmospheric flow conditions continually vary from the perpendicular flow case studied here to off-angle and nearly parallel flow that is channelled down the rows. Upstream flow conditions are then further modified by thermal stratification and terrain slope (Miller et al. 2017; Everard et al. 2020). All of these factors have a strong impact on the dynamics of the mean and turbulent flow in the CSL. In addition to increasing the complexity of cases, understanding factors relevant to plant growth such as transport of moisture and biological species or the formation of frost is of significant interest in agricultural applications. Future laboratory experiments exploring moisture and scalar transport could be performed using established and emerging methodologies (Karra et al. 2017; Shnapp et al. 2019), but capturing the full complexity of forcing conditions observed in the field most likely requires a different approach. Field studies may opt to use more advanced measurement equipment to generate spatial distributions of statistics (Van Hout et al. 2007; Nakaya et al. 2007), though this is often prohibitively expensive. Another option is to study flows using numerical simulation, which has seen great success in the past few decades and allows full control of study parameters (Stoll et al. 2020). Results presented here can be used to help understand the necessary sophistication of instrumentation and numerical models for future studies.

Supplementary Information The online version contains supplementary material available at https://doi.org/10.1007/s10546-022-00698-6.

Acknowledgements This research was supported by the National Science Foundation through grants AGS-1255662 and AGS-1660367. Funding was also provided by the United States Department of Agriculture National Institute for Food and Agriculture Specialty Crop Research Initiative Award No. 2018-03375 and the United States Department of Agriculture Agricultural Research Service through Research Support Agreement 58-2072-0-036.

References

Addepalli B, Pardyjak ER (2013) Investigation of the flow structure in step-up street canyons-mean flow and turbulence statistics. Boundary-Layer Meteorol 148(1):133–155

Bai K, Meneveau C, Katz J (2012) Near-wake turbulent flow structure and mixing length downstream of a fractal tree. Boundary-Layer Meteorol 143(2):285–308

Bai K, Katz J, Meneveau C (2015) Turbulent flow structure inside a canopy with complex multi-scale elements. Boundary-Layer Meteorol 155(3):435–457

Bailey BN, Stoll R (2013) Turbulence in sparse, organized vegetative canopies: a large-eddy simulation study. Boundary-Layer Meteorol 147(3):369–400

Bailey BN, Stoll R (2016) The creation and evolution of coherent structures in plant canopy flows and their role in turbulent transport. J Fluid Mech 789:425–460

Blackman K, Perret L, Calmet I, Rivet C (2017) Turbulent kinetic energy budget in the boundary layer developing over an urban-like rough wall using PIV. Phys Fluids 29(8):085113
Böhm M, Finnigan JJ, Raupach MR, Hughes D (2013) Turbulence structure within and above a canopy of bluff elements. Boundary-Layer Meteorol 146(3):393–419
Britter R, Hanna S (2003) Flow and dispersion in urban areas. Annu Rev Fluid Mech 35(1):469–496
Brunet Y, Finnigan JJ, Raupach MR (1994) A wind tunnel study of air flow in waving wheat: single-point velocity statistics. Boundary-Layer Meteorol 70(1):95–132
Brunet Y (2020) Turbulent flow in plant canopies: Historical perspective and overview. Boundary-Layer Meteorol 177(2):315–364
Cellier P, Brunet Y (1992) Flux-gradient relationships above tall plant canopies. Agric Meteor 58(1–2):93–117
Chahine A, Dupont S, Sinfort C, Brunet Y (2014) Wind-flow dynamics over a vineyard. Boundary-Layer Meteorol 151(3):557–577
Christen A, Rotach MW, Vogt R (2009) The budget of turbulent kinetic energy in the urban roughness sublayer. Boundary-Layer Meteorol 131(2):193–222
Cionco RM (1965) A mathematical model for air flow in a vegetative canopy. J Appl Meteor Climatol 4(4):517–522
Cionco RM (1972) A wind-profile index for canopy flow. Boundary-Layer Meteorol 3(2):255–263
Dry PR (2000) Canopy management for fruitfulness. Aust J Grape Wine Res 6(2):109–115
Dupont S, Brunet Y (2008) Edge flow and canopy structure: a large-eddy simulation study. Boundary-Layer Meteorol 126(1):51–71
Everard KA, Oldroyd HJ, Christen A (2020) Turbulent heat and momentum exchange in nocturnal drainage flow through a sloped vineyard. Boundary-Layer Meteorol 175(1):1–23
Finnigan J (2000) Turbulence in plant canopies. Annu Rev Fluid Mech 32(1):519–571
Garratt J (1980) Surface influence upon vertical profiles in the atmospheric near-surface layer. Quart J Roy Meteor Soc 106(450):803–819
Giometto M, Christen A, Meneveau C, Fang J, Krafczyk M, Parlange M (2016) Spatial characteristics of roughness sublayer mean flow and turbulence over a realistic urban surface. Boundary-Layer Meteorol 160(3):425–452
Hamed AM, Sadowski MJ, Nepf HM, Chamorro LP (2017) Impact of height heterogeneity on canopy turbulence. J Fluid Mech 813:1176–1196
Hamed AM, Peterlein AM, Speck I (2020) Characteristics of the turbulent flow within short canopy gaps. Phys Rev Fluids 5(12):123–801
Harman IN, Finnigan JJ (2007) A simple unified theory for flow in the canopy and roughness sublayer. Boundary-Layer Meteorol 123(1):339–363
Harman IN, Böhm M, Finnigan JJ, Hughes D (2016) Spatial variability of the flow and turbulence within a model canopy. Boundary-Layer Meteorol 160(3):375–396
Hayati AN, Stoll R, Pardyjak ER, Harman T, Kim JJ (2019) Comparative metrics for computational approaches in non-uniform street-canyon flows. Build Environ 158:16–27
Hong J, Katz J, Schultz MP (2011) Near-wall turbulence statistics and flow structures over three-dimensional roughness in a turbulent channel flow. J Fluid Mech 667:1–37
Hussain M, Lee BE (1980) A wind tunnel study of the mean pressure forces acting on large groups of low-rise buildings. J Wind Eng Ind Aerodyn 6(3–4):207–225
Johnson LF, Roczen DE, Youkhana SK, Nemani RR, Bosch DF (2003) Mapping vineyard leaf area with multispectral satellite imagery. Comput Electron Agric 38:33–44
Judd MJ, Raupach MR, Finnigan JJ (1996) A wind tunnel study of turbulent flow around single and multiple windbreaks, part I: Velocity fields. Boundary-Layer Meteorol 80(1–2):127–165
Kaimal JC, Finnigan JJ (1994) Atmospheric boundary layer flows: their structure and measurement. Oxford University Press, Cambridge
Karra S, Malki-Epshtein L, Neophytou MKA (2017) Air flow and pollution in a real, heterogeneous urban street canyon: A field and laboratory study. Atmos Environ 165:370–384
Laws EM, Livesey JL (1978) Flow through screens. Annu Rev Fluid Mech 10(1):247–266
Lee JP, Lee SJ (2012) PIV analysis on the shelter effect of a bank of real fir trees. J Wind Eng Ind Aerodyn 110:40–49
LeMone MA, Angevine WM, Bretherton CS, Chen F, Dudhia J, Fedorovich E, Katsaros KB, Lenschow DH, Mahrt L, Patton EG et al (2019) 100 years of progress in boundary layer meteorology. Meteor Monogr 59:9.1-9.85
Margairaz F, Eshagh H, Hayati AN, Pardyjak ER, Stoll R (2022) Development and evaluation of an isolated-tree flow model for neutral-stability conditions. Urban Clim. https://doi.org/10.1016/j.uclim.2022.101083
Maruyama T (2008) Large eddy simulation of turbulent flow around a windbreak. J Wind Eng Ind Aerodyn 96(10–11):1998–2006

Melling A (1997) Tracer particles and seeding for particle image velocimetry. Meas Sci Technol 8(12):1406–1416
Miller NE, Beresh SJ (2021) Using particle image velocimetry to determine turbulence model parameters. Am Inst Aeronaut Astronaut 59(3):842–854
Miller NE, Stoll R, Mahaffee WF, Pardyjak ER (2017) Mean and turbulent flow statistics in a trellised agricultural canopy. Boundary-Layer Meteorol 165(1):113–143
Moltchanov S, Bohbot-Raviv Y, Shavit U (2011) Dispersive stresses at the canopy upstream edge. Boundary-Layer Meteorol 139(2):333–351
Nakaya K, Suzuki C, Kobayashi T, Ikeda H, Yasuike S (2007) Spatial averaging effect on local flux measurement using a displaced-beam small aperture scintillometer above the forest canopy. Agric Meteor 145(1–2):97–109
Nebenführ B, Davidson L (2015) Large-eddy simulation study of thermally stratified canopy flow. Boundary-Layer Meteorol 156(2):253–276
Novak MD, Warland JS, Orchansky AL, Ketler R, Green S (2000) Wind tunnel and field measurements of turbulent flow in forests. part I: uniformly thinned stands. Boundary-Layer Meteorol 95(3):457–495
Park SJ, Kim JJ, Choi W, Kim ER, Song CK, Pardyjak ER (2020) Flow characteristics around step-up street canyons with various building aspect ratios. Boundary-Layer Meteorol 174(3):411–431
Patton EG, Shaw RH, Judd MJ, Raupach MR (1998) Large-eddy simulation of windbreak flow. Boundary-Layer Meteorol 87(2):275–307
Poëtte C, Gardiner B, Dupont S, Harman I, Böhm M, Finnigan J, Hughes D, Brunet Y (2017) The impact of landscape fragmentation on atmospheric flow: a wind-tunnel study. Boundary-Layer Meteorol 163(3):393–421
Poggi D, Porporato A, Ridolfi L, Albertson J, Katul G (2004) The effect of vegetation density on canopy sub-layer turbulence. Boundary-Layer Meteorol 111(3):565–587
Pope SB (2000) Turbulent Flows. Cambridge University Press, Cambridge
Raupach MR, Shaw RH (1982) Averaging procedures for flow within vegetation canopies. Boundary-Layer Meteorol 22(1):79–90
Raupach MR, Finnigan JJ, Brunei Y (1996) Coherent eddies and turbulence in vegetation canopies: the mixing-layer analogy. Boundary-Layer Meteorol 78(3–4):351–382
Shnapp R, Shapira E, Peri D, Bohbot-Raviv Y, Fattal E, Liberzon A (2019) Extended 3D-PTV for direct measurements of lagrangian statistics of canopy turbulence in a wind tunnel. Sci Rep 9(1):1–13
Speckart SO, Pardyjak ER (2014) A method for rapidly computing windbreak flow field variables. J Wind Eng Ind Aerodyn 132:101–108
Stoll R, Gibbs JA, Salesky ST, Anderson W, Calaf M (2020) Large-eddy simulation of the atmospheric boundary layer. Boundary-Layer Meteorol 177(2):1–41
Stull RB (1988) An introduction to boundary layer meteorology. Springer, Berlin
Van Hout R, Zhu W, Luznik L, Katz J, Kleissl J, Parlange MB (2007) PIV measurements in the atmospheric boundary layer within and above a mature corn canopy. part I: statistics and energy flux. J Atmos Sci 64(8):2805–2824
Yue W, Meneveau C, Parlange MB, Zhu W, Kang HS, Katz J (2008) Turbulent kinetic energy budgets in a model canopy: comparisons between les and wind-tunnel experiments. Environ Fluid Mech 8(1):73–95
Zhu W, van Hout R, Luznik L, Kang HS, Katz J, Meneveau C (2006) A comparison of PIV measurements of canopy turbulence performed in the field and in a wind tunnel model. Exp Fluids 41(2):309–318